

Electromagnetic Impact Vibration Energy Harvesters

Mohamed Bendame, Eihab Abdel-Rahman and Mostafa Soliman

Abstract Vibration energy harvesting is the focus of extensive research as an alternative power source for low-power electronic devices. First generation of vibration energy harvesters were based on linear oscillators designed to harvest vibrations in a narrow band in the vicinity of their natural frequency. However, in environments where vibrations are random or distributed over a wide spectrum, those harvesters prove ineffective. In this chapter, we present a new architecter for nonlinear vibration energy harvesters, namely the ‘Springless’ vibration energy harvesting, that can effectively harvest vibrations over a wide bandwidth and at low levels of vibration. It employs impact oscillators as the harvesting element. We study, characterize, and qualify the performance of those harvesters experimentally, analytically, and numerically.

1 Introduction

Advances in silicon electronics and MEMS technology reduced significantly the power consumption of devices, Table 1, such as wireless sensors, portable, and wearable electronics. A large number of the locations, where those devices are used, are either remote or inaccessible. Most of these low-power devices rely heavily on electrochemical batteries as a source of power. However, batteries have a limited life span and number of recharging cycles. They are also constantly in need for recharging or replacement. For applications such as wireless sensing and remote monitoring, battery replacement or recharging can be expensive, challenging or impossible in some cases. Examples include human implants, sensing devices intended for long

M. Bendame (✉) · E. Abdel-Rahman
University of Waterloo, 200 University Avenue West, N2K 4A2 Waterloo, ON, Canada
e-mail: mbendame@uwaterloo.ca

E. Abdel-Rahman
e-mail: eihab@uwaterloo.ca

M. Soliman
Department of Energy Conversion and Power Electronics,
Electronics Research Institute, Giza, Egypt
e-mail: mostafa.soliman@si-ware.com

© Springer International Publishing Switzerland 2015
M. Belhaq (ed.), *Structural Nonlinear Dynamics and Diagnosis*,
Springer Proceedings in Physics 168, DOI 10.1007/978-3-319-19851-4_2

Table 1 Selected battery-operated systems

Device type	Power consumption
Smartphone	1 W
MP3 player	50 mW
Hearing aid	1 mW
Wireless sensor	100 μ W
Cardiac pacemaker	50 μ W s
Quartz watch	5 μ W

duration, and systems that are physically placed in remote areas [1]. Another serious problem with batteries is the fact that they contain hazardous chemical materials that are harmful to the environment if not recycled. In Canada, for example, over 600 million primary consumer batteries were sold in 2007 and about 95 % of them end up in landfills [2]. With the world's growing reliance on wireless and low-power electronics and the push for a green environment, there is a great need for self-powering and self-sustaining low-power electronic devices.

The low power design trends combined with self-sustainability needs presented an opportunity for researchers to find alternative ways to power such devices and eliminate or reduce dependency on batteries. One promising avenue to achieve this goal is to exploit ambient vibration energy sources. Vibration energy harvesting technology has been making significant strides over the last few years as it aims to provide a continuous and uninterrupted source of power for low-power electronic devices and wireless sensors. While the idea of converting environmental vibration energy into electrical energy has been used before, advances in micro-electronics and low power consumption of silicon-based electronics and wireless sensors have given it an added significance.

In the research literature, the first description of an inertial micro-power-generator was an electromagnetic vibration energy harvester (VEH) presented by Williams and Yates in 1995 [3]. Since then a great deal of research has been conducted in the area of vibration energy harvesting. Earlier works by Beeby, Glynne-Jones, Roundy [4–6] and others focused on the implementation of linear oscillators to maximize the harvested energy at resonance. In this type of harvesters, the seismic mass of the VEH moves under the influence of base excitation supported by a linear spring. The oscillator attains maximum velocity, and thus input kinetic energy, in a frequency band around its natural frequency,

$$\omega = \sqrt{\frac{k}{m}}, \quad (1)$$

where k is the spring stiffness and m is the effective mass of the mechanical oscillator.

While systems in this arrangement are capable of generating electrical energy with output power on the order of few milli-Watts [6, 7], their natural frequency must be tuned to match the frequency of ambient vibrations. In fact these harvesters are

Table 2 Electromagnetic micro-power generators

Generator	f (Hz)	Accel (m/s^2)	m (g)	Power (μW)
Beeby et al. [6]	52	0.589	0.66	45
Glynne-Jones [4]	99	6.85	2.96	4990
Ching et al. [27]	110	95.5	–	830

designed to harvest at a single frequency. A high Q -factor to minimize energy losses means a very limited bandwidths over which energy can be harvested [8]. However, in environments where ambient vibrations are distributed over a wide spectrum of frequencies, with significant predominance of low frequency components, linear harvesters prove to be ineffective because of their high center frequencies and narrow bandwidth [9–11]. It is therefore impractical to use linear VEHs with relatively high center frequency (≥ 20 Hz) and narrow bandwidth to harvest ambient wideband and low frequency environmental vibrations. Examples of some linear harvesters that have been proposed over the years are listed in Table 2, a more comprehensive lists of electromagnetic energy harvesters can be found in [12]. We note that linear harvesters have high operating frequencies and low power densities. For example, the electromagnetic VIBES harvester (first line in Table 2) has a center frequency of 52 Hz and a maximum power of 45 μW .

Due to these limitations, attention in recent years has focused on the implementation of self-tuning and nonlinear systems in order to increase the vibration energy harvester's frequency bandwidth. A number of approaches have been tried for this purpose including nonlinear stiffness, resonant frequency tuning, mechanical stoppers and exploitation of nonlinear structures that display bandwidth widening behavior. These approaches lead to three main types of nonlinear vibration energy harvesters; Duffing, array, and impact harvesters.

The Duffing type harvester gets its name from the Duffing oscillator since its governing equation reduces to a Duffing equation. In this case, the nonlinearity is added to the harvester either by using nonlinear springs or by introducing magnetic forces to alter the overall system stiffness and make it appear as a nonlinear quantity in the system's model. The Duffing harvester can be classified in three categories: hardening, bistable, and softening [13]. Mann and Sims [10] presented a Duffing type harvester that uses magnetic restoring forces to levitate an oscillating center magnet. The governing equation for the harvester's mass displacement reduces to a Duffing equation, and the introduction of nonlinearities through magnetic levitation resulted in large motion over a wide band of frequencies. Using a similar approach, Mann and Owens [9] presented a nonlinear vibration energy harvester with a bistable well. Theoretical and experimental results reveal that the nonlinear generator with a bistable potential well can be used to broaden the frequency response of the harvester. The output power of the proposed harvester varied from 5 to 200 mW for input accelerations ranging from 5 to 10 m/s^2 , and from the presented results the frequency bandwidth was 1, 2, and 3 Hz for input accelerations between 5 and 6.5 m/s^2 , and

2 Hz for 10 m/s^2 respectively. Further examples of Duffing-type and other nonlinear vibration energy harvesters can be found in reviews of recently published work [8, 14, 15].

Array harvesters employ a series of mechanical resonators, usually a series of cantilever beams with varying length and center frequencies. The cantilevers are tuned in a way that all resonance frequencies are close to each other. The resonance frequencies are adjusted by tuning the geometry of each energy scavenger or by applying a proof mass. As long as the source vibration has dominant frequency within the band of the array, at least one of the beams operates at its resonance frequency. Hence, as more beams are added to the array, as much bigger is the possible bandwidth [16]. Sari et al. [17] proposed a harvester that used an array of piezoelectric oscillators made of cantilever beams on which planar gold coils were fabricated. The reported generator covers a wide band of external vibration frequencies by implementing a number of serially connected cantilevers of different lengths resulting in an array of cantilevers with varying natural frequencies. The device generates 0.4 W of continuous power in a frequency range covering a band of 800 Hz. Similar approaches were used by Lien and Shu [18] and Rezaeiasary et al. [19]. In [20], Yan et al. proposed a multi-frequency energy harvester consisting of three permanent magnets and three sets of two-layer coils supported by a beam. The idea here is that energy is harvested under the first, second, and third resonant modes.

It has been shown that impact harvesters increase the frequency bandwidth and output power of vibration energy harvesters [21–24]. Impact harvesters are realized using mechanical stoppers that limit the motion of the seismic mass. When the seismic mass impacts the stoppers, the overall stiffness of the system is reduced to a piecewise linear or nonlinear function, that results in a nonsmooth system [23]. Soliman et al. [25] proposed a wideband micropower generator that utilized a mechanical stopper placed within the stroke and the cantilever beam. When the cantilever oscillates, it engages the stopper during motion, and therefore changes its stiffness from k_1 to k_2 with ($k_1 \ll k_2$). Le Cuong et al. [26] presented a double-impact electrostatic energy harvester that used a reference device with end-stops and an impact device with movable end-stops functioning as slave transducers. The impact harvester resulted in bandwidth increase by up to a factor of 20 compared to conventional approaches.

In this chapter, we analyze a new architecture of nonlinear VEHs that uses a double-impact oscillator, namely the “Springless” VEH, as its harvesting element. Specifically, we study the response of the horizontally aligned configuration of the VEH experimentally, numerically, and analytically.

2 Springless Vibration Energy Harvester

The schematic of the “Springless” VEH, shown in Fig. 1, consists of an electromagnetic transducer and a double-impact oscillator. The oscillator is composed of an inertial mass comprising four permanent magnets residing inside a steel cage, and

Fig. 1 Schematic of the horizontally-aligned VEH

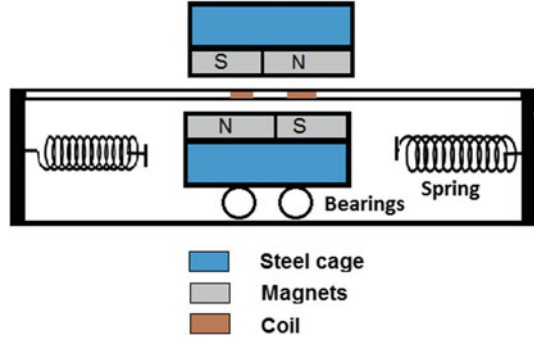
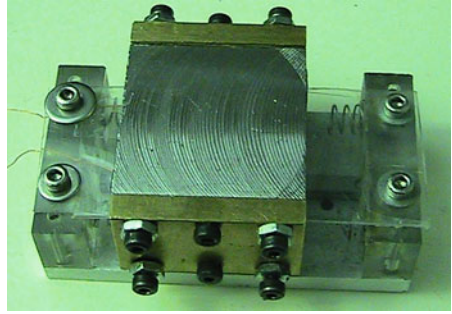


Fig. 2 Prototype of springless vibration energy harvester



two end limiters made of two identical springs attached to two resin walls at each end of the housing unit. The carriage carrying the magnetic seismic mass moves freely along the linear guide with respect to a stationary concentric coil in response to base excitations. A prototype of the VEH is shown in Fig. 2.

The motion of the magnetic carriage induces an electromotive force (emf) across the coil terminals according to Faraday's law of induction;

$$V = \frac{d\phi}{dt} \quad (2)$$

where ϕ is the total magnetic flux given by;

$$\phi = \mathbf{BA} \quad (3)$$

where \mathbf{A} is the area vector and \mathbf{B} is the magnetic field vector. For a coil that consists of N loops, the total induced voltage would be N times as large, and (2) becomes;

$$V = N \frac{d}{dt}(BA \cos \theta) \quad (4)$$

Differentiating (4) with respect to time we obtain:

$$V = N \left(\frac{dB}{dt} A \cos \theta + B \frac{dA}{dt} \cos(\theta) + BA \frac{d\theta}{dt} \right) \quad (5)$$

From (5), the harvested power depends on the magnetic field density \mathbf{B} provided by the permanent magnets, the coil's cross-section area \mathbf{A} of the coil, and the angle between the magnetic field \mathbf{B} and the normal to the coil cross section area \mathbf{A} . It is desired to maximize the output voltage by operating with an angle θ of zero and maximize the constant field density \mathbf{B} . In this case, the first and last terms of (5) will be suppressed and the equation reduces to:

$$V = NB \frac{dA}{dt} \quad (6)$$

The coil's shape is rectangular with length l and width x , during operation the length l remains constant and the width x varies with respect to the moving mass. This reduces (6) to the following:

$$V = NBl \frac{dx}{dt}, \quad (7)$$

where $\frac{dx}{dt}$ is the velocity of the moving mass.

2.1 Magnetic Field Model

One of the most important elements of the electromagnetic VEH is the magnetic flux density. It is therefore important to accurately design the magnetic circuit with the objective to maximize and stabilize the flux density around the coil. The magnetic circuit of the VEH is shown in Fig. 3, it consists of four magnets arranged as shown in the figure, a steel cage, and an air gap separating the two sets of magnets. The material for the steel cage is mild steel and the magnets are Sintered Neodymium.

The finite element modeling software ANSYS was used to determine the magnetic flux density. The FEM simulations results are compared with measured results for validation purposes. The FEM simulation results of the magnetic field strength obtained from ANSYS are shown in Figs. 4 and 5, while the measured results are shown in Fig. 6.

The measured and simulated results of the magnetic circuit show that the magnetic flux density is constant (0.74T) but has opposite signs on each side of the magnetic circuit. This is due to the fact that the polarities of the two sets of magnets are reversed (S-N and N-S). This setup allows the induced voltage across the coil to add up and hence maximize the harvested power. From Fig. 6, we recognize that the flux density is maximum over a 6–7 mm range, where it is desired that the magnets oscillate with

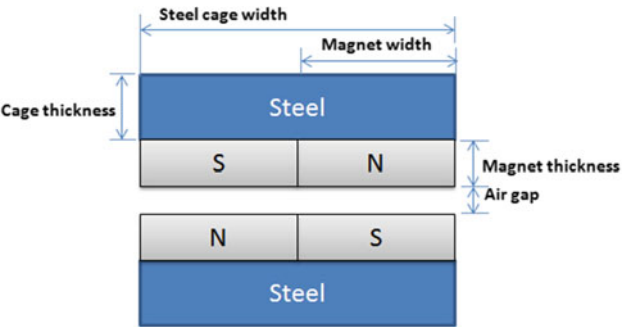


Fig. 3 Magnetic circuit

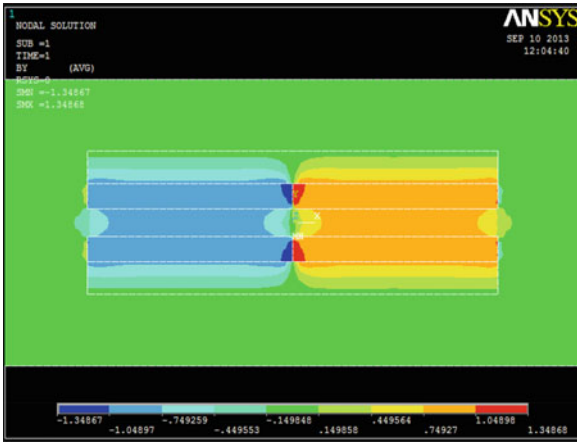


Fig. 4 Calculated magnetic flux density

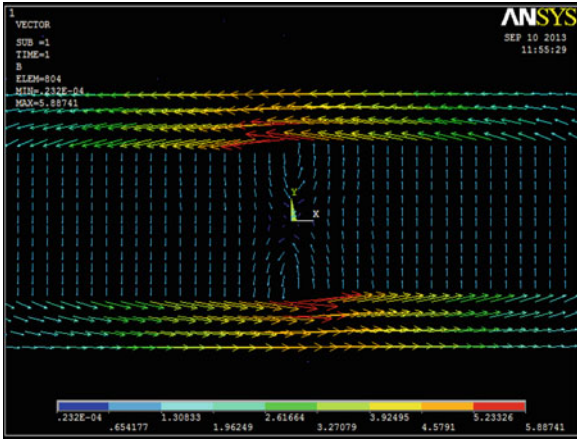
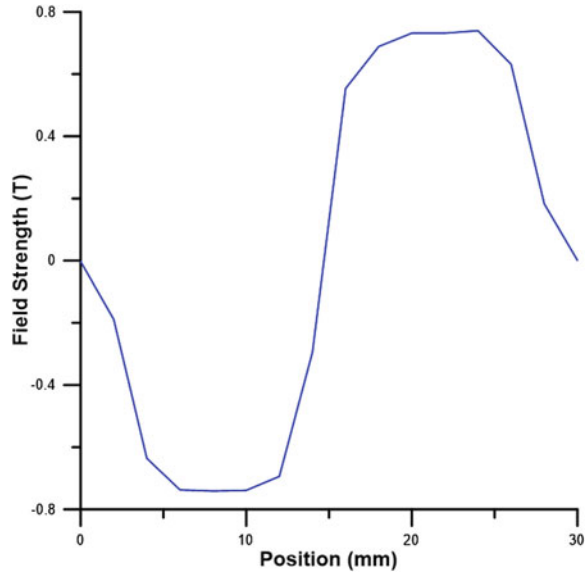


Fig. 5 Calculated magnetic field distribution

Fig. 6 Measured magnetic flux density



respect to the stationary coil in order to reduce any magnetic softening effects in the harvester.

2.2 Damping

Damping in the vibration energy harvester comes from two sources, mechanical and electrical energy losses. The mechanical damping is usually approximated as viscous linear damping, but in the case of the impact VEH cubic nonlinear damping is added to account for energy losses when the seismic mass impacts the end limiters. The cubic damping is defined as:

$$F_n = b_n \dot{x}^2 \quad (8)$$

where b_n is the nonlinear damping coefficient, and found by fitting experimental data of the frequency-response curve of the model.

2.2.1 Electrical Damping

In electromagnetic vibration energy harvesters, when the current passes through the coil it creates a magnetic field that opposes the field produced by the magnets. The interaction between the two fields produces a force which opposes the motion of the inertial mass. Consequently, the interaction force that acts as electromagnetic

damping produces the harvested power delivered to the load, and it can be expressed as [28]

$$F_{em} = b_e \frac{dx}{dt} \quad (9)$$

The electrical power is extracted from the mechanical oscillator and is given by [6]

$$P_{em} = F_{em} \frac{dx}{dt} \quad (10)$$

A small part of this power is dissipated in the coil resistance R_c , and the rest is delivered to the load resistance R_L . Equating the power dissipated to that generated by the electromagnetic force gives

$$P_{em} = b_e \left(\frac{dx}{dt} \right)^2 = \frac{V^2}{R_L + R_C + j\omega L} \quad (11)$$

where L is the coil inductance. Substituting for the voltage using (2), we can write the electromagnetic damping as

$$b_e = \frac{1}{R_L + R_C + j\omega L} \left(\frac{d\phi}{dx} \right)^2 \quad (12)$$

Assuming that the coil inductance is negligible and the magnetic field intensity B is constant, the electromagnetic damping coefficient can be expressed as:

$$b_e = \frac{(Bl)^2}{R_L + R_C} \quad (13)$$

where l is the effective length of the coil. The electrical damping can, therefore, be calculated using (13) and the parameter values given in Table 3.

2.2.2 Mechanical Damping

The viscous mechanical damping is estimated from the measured open-load frequency-response curve of the harvester, which determines the quality factor Q of the VEH, while the nonlinear damping coefficient is found by matching the experimental frequency-response curve to the numerical results of the model.

Table 3 Electromagnetic transducer parameters

Parameter	Value
Magnetic field B (T)	0.74
Effective coil length l (m)	1.75
Coil resistance R_C (Ω)	3.4

Table 4 Mechanical damping parameters

Parameter	Value
Mass, m (kg)	0.12
Stiffness, k_1 (N/m)	950
Center frequency, f_0 (Hz)	21
Low cut-off frequency, f_1 (Hz)	20.2
High cut-off frequency, f_2 (Hz)	22.5

The quality factor of the VEH is defined as:

$$Q_m = \frac{f_0}{\Delta f} \quad (14)$$

where f_0 is the center frequency and $\Delta f = f_2 - f_1$, with f_1 and f_2 are the two half-power frequencies. The quality factor relates to the mechanical damping of the harvester as follows;

$$Q_m = \frac{m \omega}{b_m} \quad (15)$$

where b_m is the mechanical damping coefficient of the open-load harvester. The mechanical damping is found using (14) and (15) and the values of the VEH's parameters given in Table 4, $b_m = 1.16$ kg/s. The center frequency and half-power bandwidth were found from a frequency-sweep curve of the base acceleration of the VEH at an amplitude of $A_0 = 0.05g$.

2.3 Gravity

The response of the VEH undergoes significant qualitative changes when the orientation of the gravitational field with respect to the linear guide changes. When the linear guide is aligned horizontal with respect to the surface of earth, such that gravity is perpendicular to the track, the harvester motions are symmetric with respect to the track mid-point. As soon as a component of the gravitational field acts along the track, it breaks the symmetry of the harvester motions.

First, in Sect. 3, the response of the symmetric HEV is analyzed when it is aligned horizontally. Then, in Sect. 4, we will model and analyze the response of the limiting case for asymmetric VEHs, a VEH aligned vertically.

3 Horizontal VEH

3.1 Model

The harvester is modeled as a single degree of freedom oscillator with piecewise-linear stiffness, Fig. 7, subject to harmonic base excitations applied directly to the housing unit.

We set the origin of the coordinate system used to describe the motion of seismic mass at the half point between the springs. The seismic mass m is assumed to be a point mass, as shown in Fig. 8. The free distance along the rail (not occupied by the cage) between the upper and lower uncompressed springs is denoted L . The uncompressed length of each spring is denoted x_s and the fully compressed length is denoted x_c . In this configuration, the governing equation of motion of the moving mass is given by:

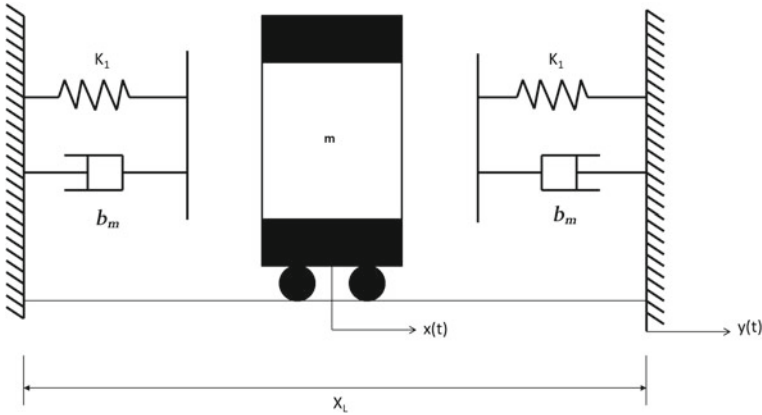
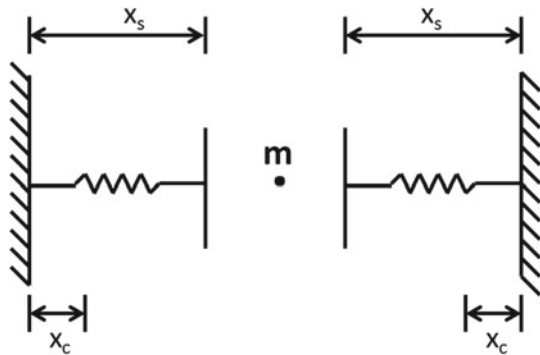


Fig. 7 Horizontal VEH schematic

Fig. 8 Horizontal VEH simplified schematic



$$m\ddot{x} + b_m\dot{x} + b_n x^2 \dot{x} + F_e + F(x) = -m\ddot{y} \quad (16)$$

where x and y are the displacements of the seismic mass m and the housing unit, respectively, and $F(x)$ is a nonsmooth function representing the system's stiffness given by (19), and F_e is the induced *emf* given by (9),

$$F_e = b_e \dot{x} \quad (17)$$

Substituting (17) in (16) we obtain the equation of motion of the “Springless” VEH;

$$m\ddot{x} + (b_m + b_e)\dot{x} + b_n x^2 \dot{x} + F(x) = -m\ddot{y} \quad (18)$$

The restoring force $F(x)$ is defined such that:

- The springs stiffness is set to the linear stiffness of the spring k_1 when it is not fully compressed (no impact)
- The springs stiffness is set to a higher stiffness k_2 when it is fully compressed (impact) with $k_2 \gg k_1$

The force-displacement relationship shown in Fig. 9, $F(x)$ can be written as follows:

$$F(x) = \begin{cases} 0 & -x_s \leq x \leq x_s \\ k_1(x - x_s) & x_s < x \leq x_c \\ k_2(x - x_c) + k_1(x_c - x_s) & x_c < x \leq \frac{L}{2} \\ k_1(x + x_s) & -x_c < x < -x_s \\ k_2(x + x_c) + k_1(x_s - x_c) & -\frac{L}{2} \leq x \leq -x_c \end{cases} \quad (19)$$

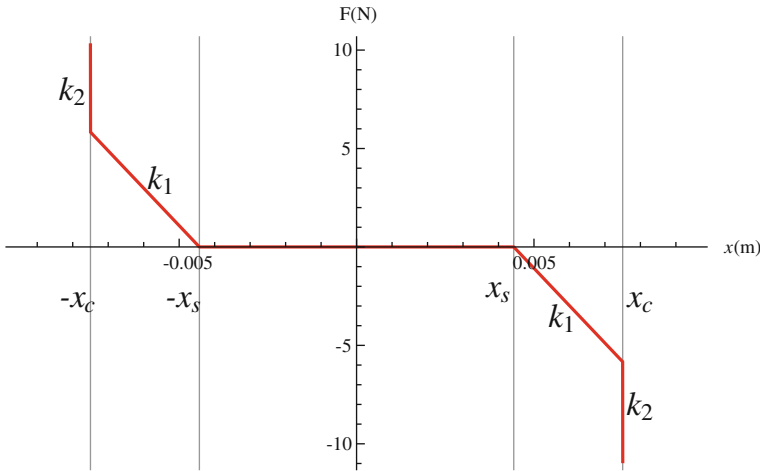


Fig. 9 Force-displacement relationship

The VEH scavenges vibration energy transmitted to it from an environmental vibration source represented by the base acceleration,

$$\ddot{y} = a(t) = A_0 \cos \omega t \quad (20)$$

where A_0 and ω are the amplitude and frequency of the external excitation. The equation of motion (18) is nondimensionalized using the nondimensional variables,

$$\begin{aligned} \omega_n &= \sqrt{\frac{k_1}{m}}, \quad \omega_h = \sqrt{\frac{k_2}{m}}, \quad \alpha_1 = \frac{x_s}{L}, \quad \alpha_2 = \frac{x_c}{L}, \quad \zeta_2 = \frac{b_n}{2m\omega_n} \\ A &= \frac{A_0}{Lm\omega_n^2}, \quad \zeta_1 = \frac{b_e + b_m}{2m\omega_n}, \quad \gamma = \left(\frac{\omega_h}{\omega_n}\right)^2, \quad \Omega = \frac{\omega}{\omega_n}. \end{aligned} \quad (21)$$

and is written as,

$$\ddot{x} = A \cos(\Omega t) - 2\dot{x}(\zeta_1 + \zeta_2 x^2) - F(x) \quad (22)$$

where the nondimensional restoring force is given by:

$$F(x) = \begin{cases} 0 & -\alpha_1 \leq x \leq \alpha_1 \\ x - \alpha_1 & \alpha_1 < x \leq \alpha_2 \\ -\alpha_1 + \alpha_2 + \gamma(x - \alpha_2) & \alpha_2 < x \leq 1 \\ \alpha_1 + x & -\alpha_2 \leq x < -\alpha_1 \\ \alpha_1 - \alpha_2 + \gamma(\alpha_2 + x) & -1 \leq x < -\alpha_2. \end{cases} \quad (23)$$

3.2 Experimental Results

The ‘‘Springless’’ VEH was tested using a feedback-controlled vibration shaker that provides base excitations with constant acceleration and different frequencies. The testing setup is shown in Fig. 10. Different experiments were performed to examine the harvesters time response and frequency response. Different time response waveforms of the VEH, shown in Fig. 11, were obtained by applying different input base excitations with constant amplitude at different frequencies, the figures show waveforms for an input amplitude $A_0 = 0.5g$ at frequencies in the region of the natural frequency of the oscillator ($f = 15, 17, 18, 20\text{Hz}$).

The frequency response curves shown in Fig. 12 represent the up and down frequency sweep for input accelerations $A_0 = 0.3 - 0.6g$ and a 40 turns concentric coil. We note from Fig. 12 a number of characteristics associated with nonlinear systems: (1) The existence of a hysteresis band between the up and down frequency sweep, (2) existence of the jump phenomena, (3) the frequency response curve peak shifts to the right as the amplitude of input excitation is increased, and (4) the frequency bandwidth increases with increase in the base excitation amplitude. We also confirm

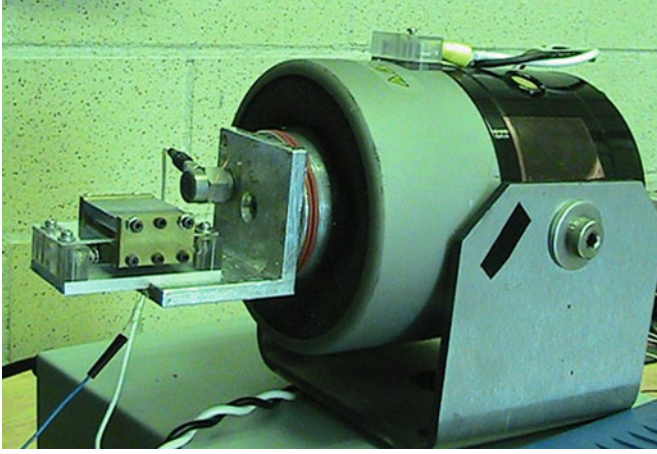
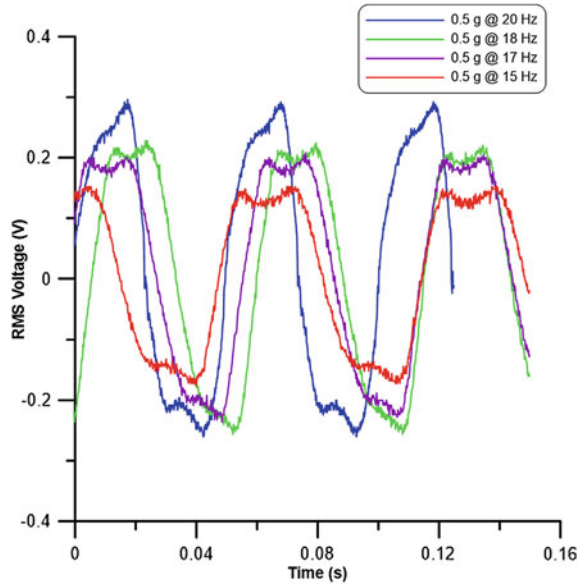


Fig. 10 Experimental setup of the horizontal “Springless” VEH

Fig. 11 Experimental time response waveforms of the “Springless” VEH for input $A_0 = 0.5g$ and frequencies $\Omega = 15, 17, 18$ and 20 Hz



from the results shown in Fig. 13 that as the coil's number of turns is increased the output voltage increases as well as the frequency bandwidth. The increase in the frequency bandwidth is due to the increase of the parasitic resistance which in turns reduces the electrical damping of the system.

Tests were carried out on the VEH to determine its optimal power and optimal load. A resistive load was connected across the coil's terminals and the base excitation input frequency was varied over the frequency range $f = 5\text{--}20$ Hz. The test was repeated

Fig. 12 VEH Experimental frequency response curves for input accelerations $A_0 = 0.3 - 0.6g$

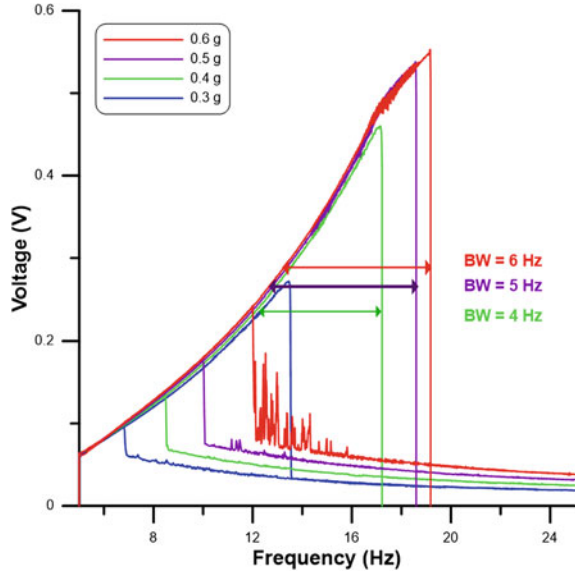
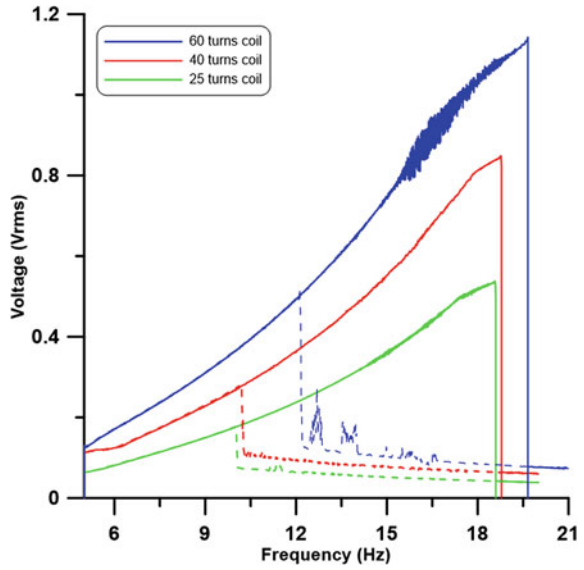
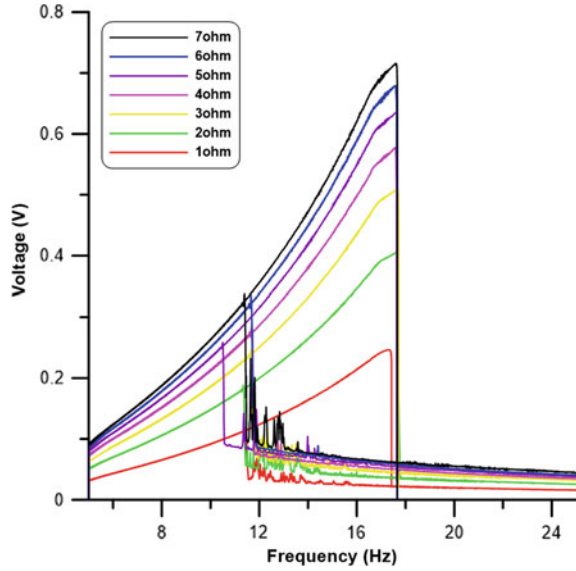


Fig. 13 Experimental frequency response curves for coils with number of turns $N = 25, 40$, and 60



using different values of the resistive load. Results shown in Fig. 14 represent the frequency-response curves of the VEH for different loads. From the figures, we conclude that the optimal power is 8.5 and 12 mW while the optimal voltage is 0.8 and 1.2 mV for a 40 and 60 turns coil respectively.

Fig. 14 Harvester's output voltage for input acceleration $A_0 = 0.5g$ and a coil with 60 turns for loads $R = 1-7 \Omega$



3.3 Numerical Results

Nonlinear dynamical systems are usually solved using numerical long-time integration. However, the long-time integration method might not yield periodic solutions easily and provides no information about the system's stability. Therefore, other numerical methods for finding periodic solutions and analyzing their stability must be used. The shooting method is a well known numerical method that uses numerical integration in conjunction with Floquet theory to obtain periodic solution and assesses their stability [29]. For validation purposes, the averaging method is used to find approximate closed-loop form solutions.

3.3.1 Shooting Method

The shooting method described in [29] is applied to the VEH equation of motion given by (18), which is written as a system of first order differential equation:

$$\begin{aligned} \dot{x}_1 &= x_2 \\ \dot{x}_2 &= -\frac{b_e + b_m}{m}x_2 - \frac{b_n}{m}x_2^2 - \frac{F_{st}(x_1)}{m} - y \end{aligned} \quad (24)$$

Equation (24) can be written as;

$$\dot{\mathbf{x}} = \mathbf{F}(\mathbf{x}, t), \quad (25)$$

where \mathbf{x} is the state variables vector (x_1, x_2) , and \mathbf{F} is a vector function. The shooting method is used to find a periodic solution, $\mathbf{x}(t) = \mathbf{x}(t + T)$, that satisfies (25) by solving the boundary-value problem:

$$\begin{aligned}\dot{\mathbf{x}} &= \mathbf{F}(\mathbf{x}, t) \\ \mathbf{x}(0) &= \eta, \mathbf{x}(T) = \eta\end{aligned}\quad (26)$$

where η is a vector of initial guesses and T is the period, both of which are in general unknown a priori. Applying the shooting technique, the two-point boundary-value problem is converted into a initial-value problem, and the resulting system of equations is

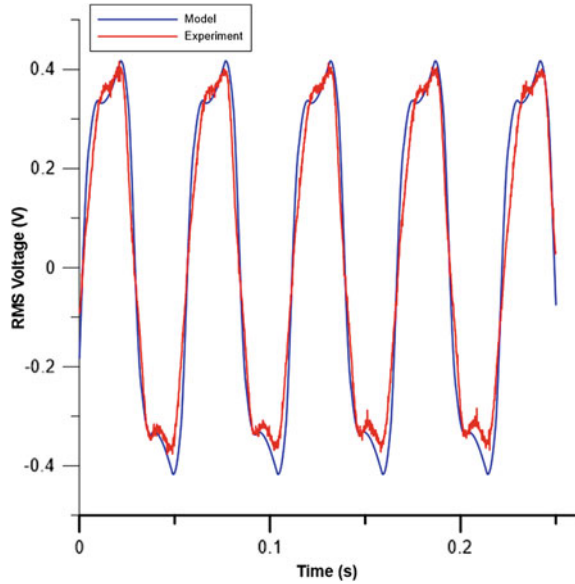
$$\begin{aligned}\dot{\mathbf{x}} &= \mathbf{F}(\mathbf{x}) \\ \mathbf{x}(0) &= \eta_0, \mathbf{x}(T) = \eta_0 \\ \frac{d}{dt} \left(\frac{\partial \mathbf{x}}{\partial \eta} \right) &= D_{\mathbf{x}} \mathbf{F}(\mathbf{x}) \frac{\partial \mathbf{x}}{\partial \eta} \\ \frac{\partial \mathbf{x}}{\partial \eta}(0) &= I\end{aligned}\quad (27)$$

where I is the two dimensional identity matrix. Applying the shooting method to our system we obtain the following system of differential equations;

$$\begin{aligned}\dot{x}_1(t) &= x_2(t) \\ \dot{x}_2(t) &= -x_2(t) \frac{b_e + b_m}{m} - x_2(t) x_1(t)^2 \frac{b_n}{m} - \frac{F_{st}}{m} - y(t) \\ \frac{d}{dt} \left(\frac{\partial x_1}{\partial \eta_1} \right) &= \frac{\partial x_2}{\partial \eta_1} \\ \frac{d}{dt} \left(\frac{\partial x_1}{\partial \eta_2} \right) &= \frac{\partial x_2}{\partial \eta_2} \\ \frac{d}{dt} \left(\frac{\partial x_2}{\partial \eta_1} \right) &= -\frac{b_e + b_m}{m} \frac{\partial x_2}{\partial \eta_1} - \frac{b_n}{m} \frac{\partial (x_2 x_1^2)}{\partial \eta_1} - \frac{1}{m} \frac{\partial F_{st}}{\partial x_1} \frac{\partial x_1}{\partial \eta_1} \\ \frac{d}{dt} \left(\frac{\partial x_2}{\partial \eta_2} \right) &= -\frac{b_e + b_m}{m} \frac{\partial x_2}{\partial \eta_2} - \frac{b_n}{m} \frac{\partial (x_2 x_1^2)}{\partial \eta_2} - \frac{1}{m} \frac{\partial F_{st}}{\partial x_1} \frac{\partial x_1}{\partial \eta_2} \\ \mathbf{x}(0) &= \eta_0 \\ \frac{\partial x_1}{\partial \eta_1}(0) &= 1, \frac{\partial x_1}{\partial \eta_2}(0) = 0, \frac{\partial x_2}{\partial \eta_1}(0) = 0, \frac{\partial x_2}{\partial \eta_2}(0) = 1\end{aligned}\quad (28)$$

The shooting algorithm requires an initial guess, this is done by solving (24) by long time integration for a given base acceleration amplitude and frequency, then a point on the obtained orbit is used as an initial guess to solve the system of (27). A periodic solution is found once the change in the initial guess between two iterations falls within a predefined error criteria. The amplitude or frequency

Fig. 15 Harvester's experimental and model output voltage for input acceleration $A_0 = 0.5g$ and frequency $f = 18\text{ Hz}$, and a coil with 60 turns



of base acceleration is then updated and the process is repeated to obtain an orbit corresponding to the new forcing parameters. Figure 15 shows the waveforms of the VEH obtained numerically and experimentally. From the figure we note a very close match between numeric and experimental results. Figure 16 shows the numeric and experimental frequency response curves of the VEH. The numerical results match those experimentally indicating the model captures and reproduces the behavior of the VEH.

3.4 Analytical Results

The averaging method is used to obtain an approximate closed-form solution of the harvester's equation of motion given by (18). We assume a solution of the form:

$$x(t) = a \sin(\Omega t + \beta) \quad (29)$$

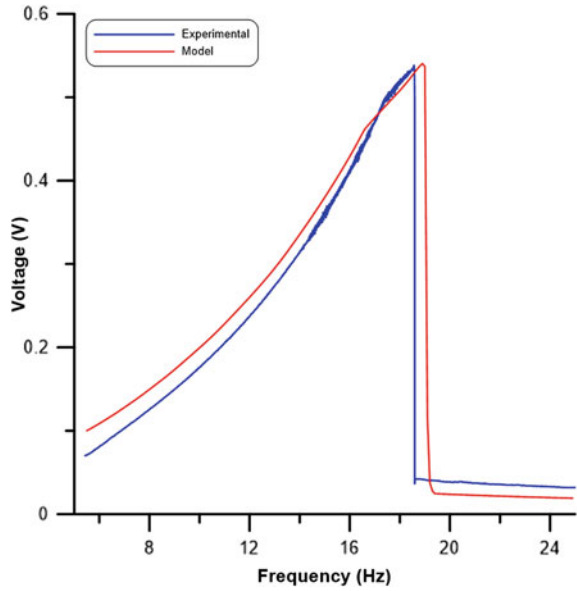
where a and β are slowly varying amplitude and phase. We also assume that:

$$\dot{x}(t) = a\Omega \cos(\Omega t + \beta) \quad (30)$$

subject to the constraint:

$$\dot{a} \sin \phi + a\dot{\beta} \cos \phi = 0. \quad (31)$$

Fig. 16 VEH's experimental and numerical frequency response curves for input acceleration $A_0 = 0.5g$ and a coil with 60 turns



where we set $\phi = \Omega t + \beta$. Using (29) and (30) in the normalized equation of motion (18), we obtain the second constraint:

$$\begin{aligned} \dot{a} \cos \phi + 2a\zeta \cos \phi ((1 + a^2) \sin(t + \beta))^2 + F(x) \\ = a(\dot{\beta} + 1) \sin \phi + A \cos(\Omega t). \end{aligned} \quad (32)$$

Solving (31) and (32) for \dot{a} and $\dot{\beta}$ yields:

$$\dot{a} = -[2a\zeta \cos \phi (1 + a^2 \sin^2 \phi) - a \sin(\phi) - A \cos(\Omega t) + F(\phi)] \cos \phi \quad (33)$$

$$a\dot{\beta} = [2a\zeta \cos(\phi) (1 + a^2 \sin^2 \phi) - a \sin(\phi) - A \cos(\Omega t) + F(\phi)] \sin(\phi) \quad (34)$$

Next, we use (29) to write the restoring force in terms of the phase angle ϕ as

$$F(\phi) = \begin{cases} 0 & 0 \leq \phi \leq \phi_1 \\ a \sin \phi - \alpha_1 & \phi_1 \leq \phi \leq \phi_2 \\ a\gamma \sin \phi + \alpha_2(1 - \gamma) - \alpha_1 & \phi_2 \leq \phi \leq \pi - \phi_2 \\ 0 & \pi - \phi_1 \leq \phi \leq \phi_1 + \pi \\ a \sin \phi + \alpha_1 & \phi_1 + \pi \leq \phi \leq \phi_2 + \pi \\ a\gamma \sin \phi + \alpha_2(\gamma - 1) + \alpha_1 & \phi_2 + \pi \leq \phi \leq 2\pi - \phi_2 \\ a \sin \phi + \alpha_1 & 2\pi - \phi_2 \leq \phi \leq 2\pi - \phi_1 \\ 0 & 2\pi - \phi_1 \leq \phi \leq 2\pi \end{cases} \quad (35)$$

where

$$\phi_1 = \sin^{-1} \left(\frac{\alpha_1}{a} \right), \quad \phi_2 = \sin^{-1} \left(\frac{\alpha_2}{a} \right)$$

are the phase angles corresponding the seismic mass contacting the linear spring at $x = x_s$ and the fully compressed spring $x = x_c$, respectively.

We define a detuning parameter describing the difference between the forcing frequency Ω and ω_n as

$$\sigma = \Omega - 1$$

and average (33) and (34) over the interval of one period $(0, 2\pi)$ to obtain the modulation equations

$$\begin{aligned} \dot{a} &= -a \frac{1}{2} \zeta (4 + a^2) + \frac{A}{2} \cos(\sigma t - \beta) \\ \dot{\beta} &= \frac{1}{2\pi} \left[-2\alpha_2(\gamma - 1) \sqrt{1 - \frac{\alpha_2^2}{a^2}} - 2\alpha_1 \sqrt{1 - \frac{\alpha_1^2}{a^2}} \right. \\ &\quad \left. + a \left(-2(\gamma - 1) \sin^{-1} \left(\frac{\alpha_2}{a} \right) - 2 \sin^{-1} \left(\frac{\alpha_1}{a} \right) + \pi \gamma \right) \right] - \frac{1}{2} \\ &\quad - \frac{A}{2a} \sin(\sigma t - \beta) \end{aligned} \quad (36)$$

Defining the phase angle $\psi = \sigma t - \beta$, we write the modulation equations in autonomous form as

$$\begin{aligned} \dot{a} &= -a \frac{1}{2} \zeta (4 + a^2) + \frac{A}{2} \cos \psi \\ \dot{\psi} &= \sigma - \frac{1}{2\pi} \left[2\alpha_2(\gamma - 1) \sqrt{1 - \frac{\alpha_2^2}{a^2}} + 2\alpha_1 \sqrt{1 - \frac{\alpha_1^2}{a^2}} \right. \\ &\quad \left. + a \left(-2(\gamma - 1) \sin^{-1} \left(\frac{\alpha_2}{a} \right) - 2 \sin^{-1} \left(\frac{\alpha_1}{a} \right) + \pi \gamma \right) \right] - \frac{1}{2} \\ &\quad - \frac{A}{2a} \sin \psi \end{aligned} \quad (37)$$

The steady-state periodic solutions correspond to the fixed points (a_0, ψ_0) of the modulation equations. These equations are solved numerically for the fixed points as a function of the detuning parameter σ . Substituting the fixed point at $\sigma = 0$, which corresponds to the resonance frequency, in the assumed solution form, (29), we obtain the seismic mass response shown in Figs. 17 and 18. Figure 17 shows the time response of the seismic mass displacement when the frequency of base excitation matches the natural frequency of the oscillator. Figure 18 shows the corresponding orbits of the seismic mass obtained numerically and analytically.

4 Vertical Configuration

A vertical implementation of the VEH, is suitable for environments where motions are predominantly in the vertical direction. The linear guide, aligned vertically as shown in Fig. 19, allows the carriage to move freely along the rail. When the assembly vibrates due to a base excitation $y(t)$, the seismic mass m moves with respect to the housing producing a relative displacement $x(t)$. In this section the mathematical model of the vertically aligned VEH is derived and the numerical method used to obtain the periodic orbits of the system. Experimental results are then used to validate the model.

Fig. 17 Displacement of VEH's mass m : numerical (red) and analytical (blue) for base acceleration amplitude of $A_0 = 0.6g$

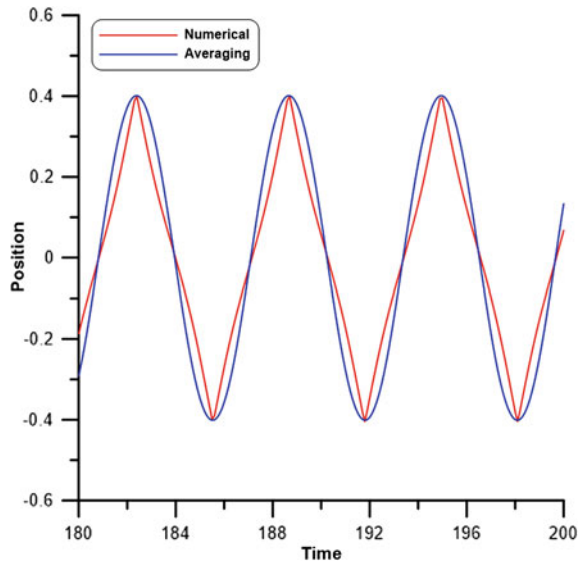


Fig. 18 VEH orbits: numerical (blue) and averaging (green) for base acceleration amplitude of $A_0 = 0.6g$

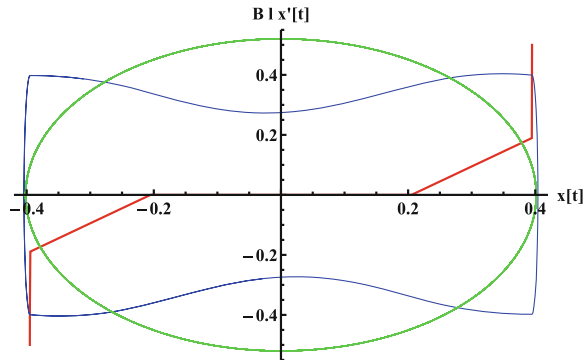
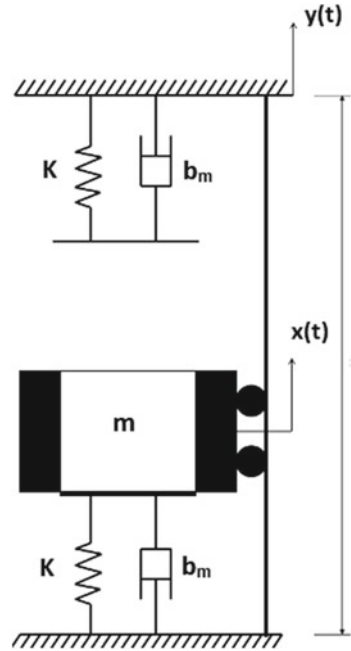


Fig. 19 Schematic of the vertically-aligned springless VEH



4.1 Model

The equation of motion of the vertically-aligned harvester can be written as:

$$m\ddot{x} = -(b_e + b_m) \dot{x} - F_{st}(x) - m\ddot{y} - mg, \quad (38)$$

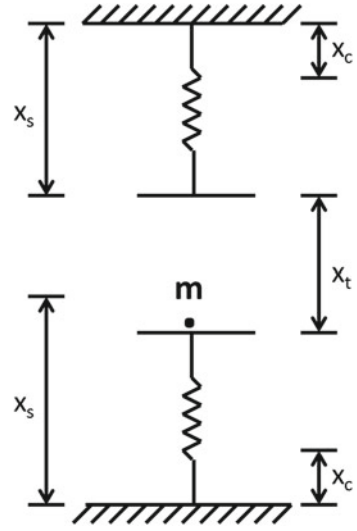
where $F_{st}(x)$ is the restoring force. The VEH harvests kinetic energy transmitted to it from the host vibrations represented by the base acceleration

$$\ddot{y} = A_0 \cos(\Omega t), \quad (39)$$

where A_0 and Ω are the amplitude and frequency of the external excitation.

The origin of the coordinate system is placed at the point where mass m rests on the lower spring. The seismic mass m is assumed to be a point mass, as shown in Fig. 20. The free distance along the rail, not occupied by the cage, between the upper and lower uncompressed springs is denoted x_t . The uncompressed length of each spring is denoted x_s and the fully compressed length is denoted x_c . The restoring force $F_{st}(x)$ varies with the position of the inertial mass m according to the equation:

Fig. 20 Simplified schematic of the VEH



$$F_{st}(x) = \begin{cases} 0 & 0 \leq x \leq x_t \\ k_1 x & x_c - x_s < x \leq 0 \\ k_1(x_c - x_s) + k_2(-x_c + x_s + x) & -x_s \leq x \leq x_c - x_s \\ k_1(x - x_t) & x_t < x < -x_c + x_s + x_t \\ k_1(x_s - x_c) + k_2(x_c - x_s - x_t + x) & -x_c + x_s + x_t < x < x_s + x_t \end{cases} \quad (40)$$

where x_s is the position where the mass touches the uncompressed spring, x_c is the position where the spring is fully compressed, k_1 is the linear spring stiffness, and k_2 the linear stiffness of the fully compressed spring. The force-displacement relationship is shown in Fig. 21.

5 Results

A prototype of the VEH is mounted on an electromagnetic shaker as shown in Fig. 22 and a base acceleration is applied as input excitation with amplitude A_0 and frequency Ω . The voltage across the coil terminals is measured using an oscilloscope.

Experimental results show that the vertically-aligned harvester possesses three different regions of operation. For amplitudes ($A_0 \leq 0.05g$), the VEH response is linear, since the seismic mass remains attached to the lower spring throughout motion, this region will be known as the linear regime. For acceleration amplitudes in the range ($0.1g < A_0 < 0.5g$), the mass detaches from the lower spring during motion without impacting the upper one. In this region, the response is that of a

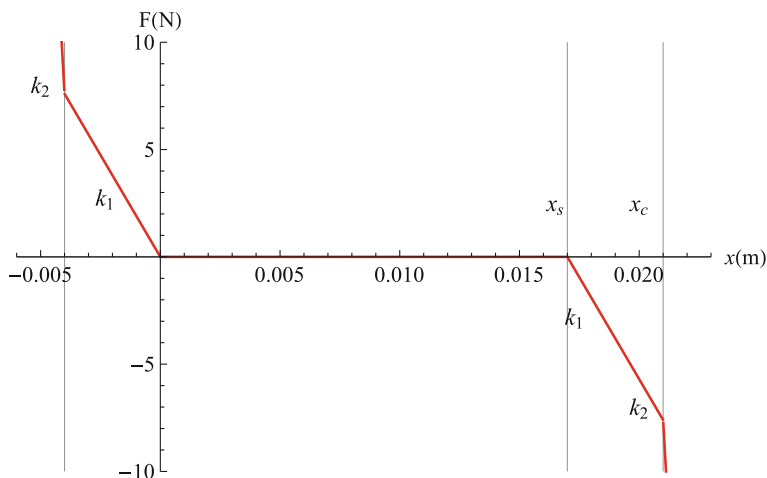
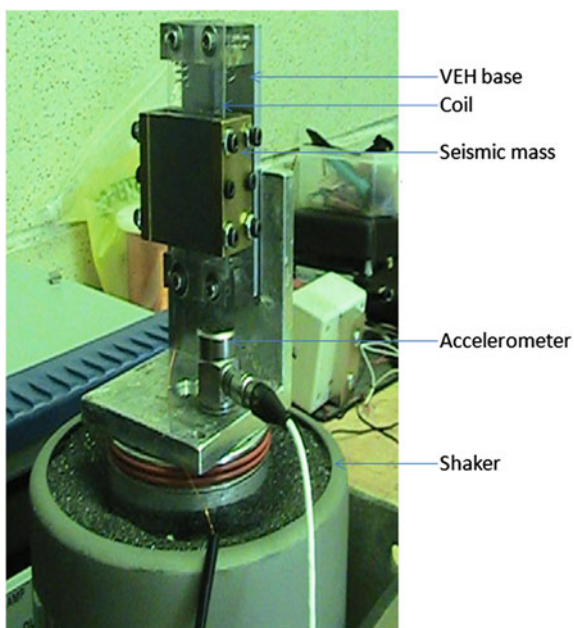


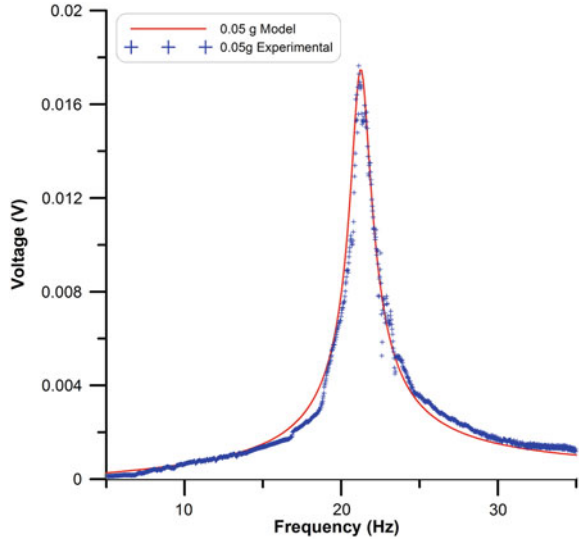
Fig. 21 Restoring force-displacement relationship

Fig. 22 Experimental setup of the VEH



single-impact oscillator and will be therefore called the single impact regime. For acceleration amplitudes ($A_0 > 0.5g$), the mass impacts both springs and the response is that of a double-impact oscillator, this will be called the double impact regime. The experimental and numerical results for the three different regimes are presented next.

Fig. 23 The numerical (*red line*) and experimental (*blue +*) open circuit voltage (RMS) for an excitation of amplitude $A_0 = 0.03g$ (Color figure Online)



5.1 Linear Regime

In this case, the mass remains in contact with the lower spring. Test results show that the response of the VEh is linear. Figure 23 shows the measured and numerically obtained frequency-response curves of the voltage (RMS) across the open circuit terminals of the coil. Base acceleration amplitude is held constant at $A_0 = 0.03g$, while the frequency is swept up and down in the range 12–30 Hz.

Since the response of the VEh system is linear, the piecewise restoring force reduces to a linear relationship between stiffness and displacement, and the equation of motion is reduced to a simple spring-mass-damper model given by:

$$\ddot{x} = -\frac{b_m}{m} \dot{x} - \frac{k_1}{m} x - \ddot{y} - g, \quad (41)$$

The steady-state response x of linear model under a base acceleration

$$\ddot{y} = \Omega^2 Y_0 \cos \Omega t = A_0 \cos \Omega t \quad (42)$$

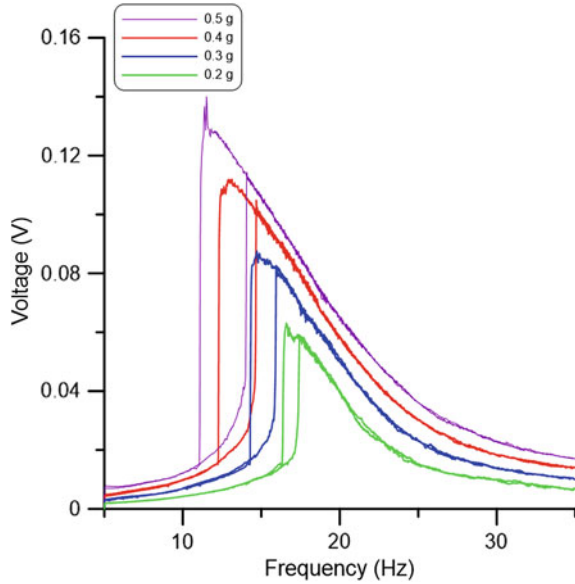
is given by:

$$x(t) = a \cos(\Omega t + \Phi) \quad (43)$$

where a and Φ are the amplitude and phase of the system response and their expressions can be found in books that deal with linear one DOF oscillators. The open circuit voltage is given by:

$$V_L = B l \dot{x} \quad (44)$$

Fig. 24 Frequency-response curves of the VEH under base acceleration amplitudes in the range of $A_0 = 0.2\text{--}0.5g$



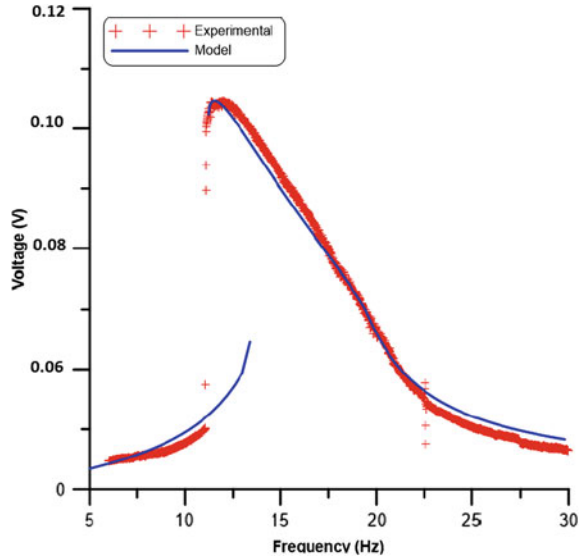
The harvester's response is obtained by substituting the parameter values listed in Table 4 into (41) and numerically integrating. The results, shown in Fig. 23, agree reasonably well with the experimental results. The maximum output voltage is 18 mV obtained at the center frequency $f_c = 21$ Hz and the harvesting bandwidth is 3 Hz.

5.2 Single Impact

The experimental frequency-response curves of the voltage across the open circuit terminals of the coil for base acceleration amplitudes in the range 0.2–0.5 g are shown in Fig. 24. The figure shows the up- and down-sweeps in the frequency range 5–35 Hz. We note the existence of hysteresis between the up and down frequency sweeps and jumps between an upper and a lower branches of response in the frequency-response curves. We note in Fig. 24 that the jump to the lower branch occurs as the frequency is swept down indicating the existence of a softening nonlinearity in the VEH [29]. The hysteresis range increases with base acceleration amplitude from 1 Hz at $A_0 = 0.2g$ –3 Hz at $A_0 = 0.5g$.

The harvester response for a base acceleration amplitude $A_0 = 0.4g$ was obtained numerically and the results compare reasonably well with the experimental results as shown in Fig. 25. The stiffness and damping were reduced for this regime to $k_1 = 880$ N/m and $b_m = 0.6$ N m/s, respectively. This is expected since in this regime the mass loses contact with the spring and spends significant time in air and thus reducing the effective stiffness and damping of the VEH.

Fig. 25 The open circuit voltage between the coil terminals for a base acceleration amplitude $A_0 = 0.4g$



We note that the reduction in effective stiffness shifts the center frequency from $f_c = 21$ Hz to the range 12–16.5 Hz, which indicates that nonlinearities in the system facilitate low frequency harvesting. Further, as the base acceleration amplitude was increased, the peak frequency dropped, from $f_c = 16.5$ Hz at $A_0 = 0.2g$ – $f_c = 14.5$ Hz at $A_0 = 0.3g$ and $f_c = 12$ Hz at $A_0 = 0.4g$, as the carriage spent more time in air away from the lower spring.

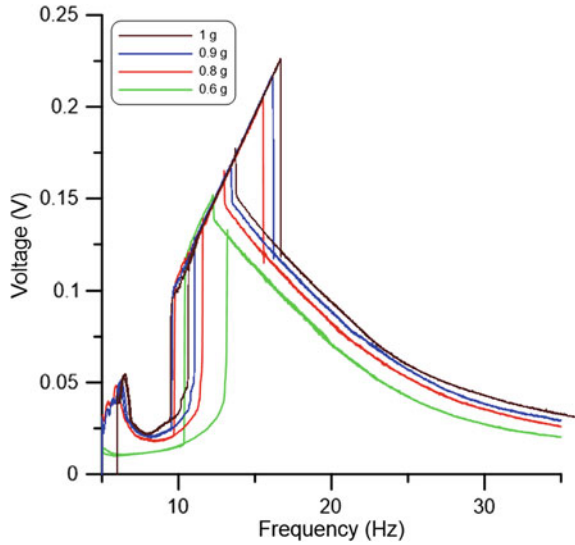
Meanwhile, the maximum output voltage continued to increase with base acceleration amplitude as expected. For base acceleration amplitude $A_0 = 0.4g$, the maximum output voltage was 110 mV (RMS) obtained at a frequency of $f_c = 12$ Hz.

5.3 Double Impact

For large excitations, the base acceleration amplitude was set to the range of $A_0 = 0.6 - 1g$. Figure 26 shows the frequency-response curves obtained for the open-circuit output voltage of the VEH. As in the case of moderate excitations, note the up and down jumps between branches of response and hysteresis between up and down-sweeps in the frequency range of 5–35 Hz.

We also observe a new branch of responses in the harvester frequency response. Two additional jumps appear to the right (at higher frequency) of the two original jumps in the frequency-response curves leading up to the new branch during frequency down-sweeps and down from it during up-sweeps. The harvester response is linear along this new branch. For instance, for base acceleration amplitude $A_0 = 0.8g$ the new jumps occur at $f = 13$ and $f_c = 15$ Hz.

Fig. 26 Frequency-response curves of the VEH for base acceleration amplitude in the range of $A_0 = 0.6\text{--}1g$



This new phenomenon is attributed to large seismic mass motions covering the entire track between the two springs. Along this branch of response, the mass motions reach the maximum allowable displacement

$$D \approx x_t + x_s - x_c$$

which remains almost constant as the excitation frequency varies since it is limited by the two hard springs k_2 . As a result, the velocity along this branch is

$$\dot{x} \approx \omega D \sin(\omega t + \phi)$$

Using (44), we obtain the output voltage (RMS) as

$$V = \frac{BID}{\sqrt{2}} \omega \quad (45)$$

We note that the measured output voltage varies linearly with the frequency, Fig. 26, in accordance with (45). Further, since base acceleration amplitude does not appear in (45), the voltage output falls on the same line for all acceleration amplitude values reported here.

6 Conclusion

In this paper we investigated the response of a wideband impact VEH numerically and experimentally when aligned horizontally and vertically. Results show that using a double-impact oscillator and a concentric coil enhanced the harvester's output power and its bandwidth. A maximum output power of 12 mW over a frequency bandwidth $BW = 6$ Hz was achieved using a 60 turns coil with an effective length $l = 1.75$ m and a 3.6Ω , from an input acceleration $A_0 = 0.6g$. We also note that the impact produced a hardening/softening type nonlinearity in the horizontal/vertical configuration of VEH. The VEH's bandwidth increased with increase of the input acceleration and an increase in the number of turns in the concentric coil. Numerical analysis of the VEH show the existence of nonlinear phenomena that are reminiscent of impact oscillator, in particular, the jump phenomena in the frequency response of the VEH and the existence of hysteresis.

References

1. Arnold, D.P.: Review of microscale magnetic power generation. *J. IEEE Trans. Matwo Magn.* **43**, 3940–3951 (2007)
2. www.ec.gc.ca/gdd-mw/default.asp?lang=En&n=52DF915F-1&offset=1&toc=show
3. Williams, C.B., Yates, R.B.: Analysis of a micro-electric generator for microsystems. *Solid State Sens. Actuators* **1**, 369–372 (1996)
4. Glynne-Jones, P.: Vibration powered generators for self-powered microsystems, University of Southampton, PhD Thesis (2001)
5. Roundy, S., Leland, E.S., Baker, J.: Improving power output for vibration-based energy scavengers. *J. Pervasive Comput. IEEEExplore* (2005)
6. Beeby, S.P., O'Donnell, T.: Chapter 5, pp. 130–132, in energy harvesting technology. In: Priya, S., Inman, D.J.(eds.) Springer, New York (2009)
7. Hadas, Z., Kluge, M., Singule, V., Ondrusek, C.: Electromagnetic vibration power generator. *IEEE* (2007)
8. Zhu, D., Beeby, S.: *Energy Harvesting Systems*, Springer, ISBN 978-1-4419-7565-2 (2011)
9. Mann, B.P., Owens, B.A.: Investigations of a nonlinear energy harvester with a bistable potential well. *J. Sound Vib.* **329**, 1215–1226 (2010)
10. Mann, B.P., Sims, N.D.: Energy harvesting from the nonlinear oscillations of magnetic levitation. *J. Sound Vib.* **319**, 515–530 (2009)
11. Cammarano, A., Burrow, S.G., Barton, D.A.W.: An energy harvester with bistable compliance characteristics, DETC2010-29222. In: 12th International Conference on Advanced Vehicle and Tire Technologies; 4th International Conference on Micro- and Nanosystems, vol. 4, pp. 725–732. publisher Asme (2010)
12. Gilbert, J.M., Balouchi, F.: Comparison of energy harvesting systems for wireless sensor networks. *Int. J. Autom. Comput.* **5**, 334–347 (2008)
13. Duy, S.N., Einar, H.: Wideband MEMS energy harvester driven by colored noise. *J. Micro-electromech. Syst. IEEE* **22**(4) (2013)
14. Harne, R., Wang, K.: A review of the recent research on vibration energy harvesting via bistable systems. *J. Smart Mater. Struct.* **22** (2008)
15. Daqaq, M.F., Masana, R., Erturk, A., Dane, Q.: On the role of nonlinearities in vibratory energy harvesting: a critical review and discussion. *J. Appl. Mech. Rev.* **66** (2014)
16. Twiefel, J., Westermann, H.: *J. Intell. Mater. Syst. Struct.* **24**, 1291–1302 (2013)

17. Sari, I., Balkan, T., Kulah, H.: An electromagnetic micro power generator for wideband environmental vibrations. *J. Micromech. Microeng.* **146**, 405–413 (2008)
18. Lien, I., Shu, Y.: Array of piezoelectric energy harvesting by equivalent impedance approach, *J. Smart Mater. Struct.* **21** (2012)
19. Rezaeiasary, M., El Gowini, M., Sameoto, D., Raboud, D., Moussa, W.: Wide-bandwidth piezoelectric energy harvester with polymeric structure. *J. Micromech. Microeng.* **25** (2004)
20. Yang, B., Lee, C., Xiang, W., Xie, J., Han He, J., Kotlanka, R.K., Low, S.P., Feng, H.: Electromagnetic energy harvesting from vibrations of multiple frequencies. *J. Micromech. Microeng.* **19** (2009)
21. Dhakar, L., Liu, F.E.H., Tay, F.E., Lee, C.: A new energy harvester design for high power output at low frequencies. *J. Sens. Actuators* **199**, 344–352 (2013)
22. Lihua, T., Yaowen, Y., Soh, C.K.: *Broadband Vibration Energy Harvesting Techniques*. Springer, New York (2013)
23. Soliman, M.S., Abdel-Rahman, E., El-Saadany, E., Mansour, R.R.: A wideband vibration-based energy harvester. *J. Micromech. Microeng.* **18**, 1257–1265 (2008)
24. Jacquelin, E., Adhikari, S., Friswell, M.: A piezoelectric device for impact energy harvesting. *J. Smart Mater. Struct.* **20**, 1–12 (2011)
25. Soliman, M.S., Abdel-Rahman, E., El-Saadany, E., Mansour, R.R.: A design procedure for wideband micropower generators. *J. Microelectromech. Syst.* **18**, 1288–1299 (2009)
26. Le, C.P., Halvorsen, E.: MEMS electrostatic energy harvesters with end-stop effects. *J. Micromech. Microeng.* **22**, 074013 (2012)
27. Ching, N.H., Wong, H.Y., Li, H.W.J., Leong, P.H.W., Wen, Z.: A laser-micromachined multimodal resonating power transducer for wireless sensing systems. *J. Sens. Actuators* **97–98** (2002)
28. Mahmoud, M.A.E., Abdel-Rahman, E.M., Mansour, R.R., El-Saadany, E.F.: Springless vibration energy harvesters. In: *ASME IDETC 2010, Montreal, Canada, DETC2010-29046*, Aug 2010
29. Nayfeh, A., Mook, D.: *Nonlinear Oscillations*. Wiley, New York (1997)

Structural Nonlinear Dynamics and Diagnosis

Selected papers from CSNDD 2012 and CSNDD 2014

Belhaq, M. (Ed.)

2015, XIV, 509 p. 265 illus., 13 illus. in color., Hardcover

ISBN: 978-3-319-19850-7